

Highly sensitive detection of cancer cells using femtosecond dual-wavelength near-IR two-photon imaging

Jean R. Starkey,^{1,*} Nikolay S. Makarov,^{2,3} Mikhail Drobizhev,² and Aleksander Rebane^{2,4}

¹Department of Microbiology, Montana State University, Bozeman, MT 59717, USA

²Department of Physics, Montana State University, Bozeman, MT 59717, USA

³Currently with Department of Chemistry and Biochemistry, Georgia Institute of Technology, GA 30332, USA

⁴National Institute of Chemical Physics and Biophysics, Tallinn, 12618, Estonia

*umbjs@montana.edu

Abstract: We describe novel imaging protocols that allow detection of small cancer cell colonies deep inside tissue phantoms with high sensitivity and specificity. We compare fluorescence excited in Styryl-9M molecules by femtosecond pulses at near IR wavelengths, where Styryl-9M shows the largest dependence of the two-photon absorption (2PA) cross section on the local environment. We show that by calculating the normalized ratio of the two-photon excited fluorescence (2PEF) intensity at 1200 nm and 1100 nm excitation wavelengths we can achieve high sensitivity and specificity for determining the location of cancer cells surrounded by normal cells. The 2PEF results showed a positive correlation with the levels of MDR1 proteins expressed by the cells, and, for high MDR1 expressors, as few as ten cancer cells could be detected. Similar high sensitivity is also demonstrated for tumor colonies induced in mouse external ears. This technique could be useful in early cancer detection, and, perhaps, also in monitoring dormant cancer deposits.

© 2012 Optical Society of America

OCIS codes: (170.3880) Medical and biological imaging; (190.4180) Multiphoton processes.

References and links

1. M. Solomon, Y. Liu, M. Y. Berezin, and S. Achilefu, "Optical imaging in cancer research: basic principles, tumor detection, and therapeutic monitoring," *Med. Princ. Pract.* **20**(5), 397–415 (2011).
2. J. M. Song, R. Jagannathan, D. L. Stokes, P. M. Kasili, M. Panjehpour, M. N. Phan, B. F. Overholt, R. C. DeNovo, X. Pan, R. J. Lee, and T. Vo-Dinh, "Development of a fluorescence detection system using optical parametric oscillator (OPO) laser excitation for *in vivo* diagnosis," *Technol. Cancer Res. Treat.* **2**(6), 515–523 (2003).
3. P. S. Adusumilli, D. P. Eisenberg, Y. S. Chun, K. W. Ryu, L. Ben-Porat, K. J. Hendershot, M. K. Chan, R. Huq, C. C. Riedl, and Y. Fong, "Virally directed fluorescent imaging improves diagnostic sensitivity in the detection of minimal residual disease after potentially curative cytoreductive surgery," *J. Gastrointest. Surg.* **9**(8), 1138–1147 (2005).
4. M. T. Weigel and M. Dowsett, "Current and emerging biomarkers in breast cancer: prognosis and prediction," *Endocr. Relat. Cancer* **17**(4), R245–R262 (2010).
5. K. Licha, C. Hessenius, A. Becker, P. Henklein, M. Bauer, S. Wisniewski, B. Wiedenmann, and W. Semmler, "Synthesis, characterization, and biological properties of cyanine-labeled somatostatin analogues as receptor-targeted fluorescent probes," *Bioconjug. Chem.* **12**(1), 44–50 (2001).
6. S. Achilefu, "Lighting up tumors with receptor-specific optical molecular probes," *Technol. Cancer Res. Treat.* **3**(4), 393–409 (2004).
7. S. Kukreti, A. E. Cerussi, W. Tanamai, D. Hsiang, B. J. Tromberg, and E. Gratton, "Characterization of metabolic differences between benign and malignant tumors: high-spectral-resolution diffuse optical spectroscopy," *Radiology* **254**(1), 277–284 (2010).
8. J. E. Bugaj, S. Achilefu, R. B. Dorshow, and R. Rajagopalan, "Novel fluorescent contrast agents for optical imaging of *in vivo* tumors based on a receptor-targeted dye-peptide conjugate platform," *J. Biomed. Opt.* **6**(2), 122–133 (2001).

9. S. Achilefu, R. B. Dorshow, J. E. Bugaj, and R. Rajagopalan, "Novel receptor-targeted fluorescent contrast agents for *in vivo* tumor imaging," *Invest. Radiol.* **35**(8), 479–485 (2000).
10. L. Josephson, M. F. Kircher, U. Mahmood, Y. Tang, and R. Weissleder, "Near-infrared fluorescent nanoparticles as combined MR/optical imaging probes," *Bioconjug. Chem.* **13**(3), 554–560 (2002).
11. F. B. Haeussinger, S. Heinzel, T. Hahn, M. Schecklmann, A. C. Ehli, and A. J. Fallgatter, "Simulation of near-infrared light absorption considering individual head and prefrontal cortex anatomy: implications for optical neuroimaging," *PLoS ONE* **6**(10), e26377 (2011).
12. C. G. Hadjipanayis, H. Jiang, D. W. Roberts, and L. Yang, "Current and future clinical applications for optical imaging of cancer: from intraoperative surgical guidance to cancer screening," *Semin. Oncol.* **38**(1), 109–118 (2011).
13. N. Almog, "Molecular mechanisms underlying tumor dormancy," *Cancer Lett.* **294**(2), 139–146 (2010).
14. O. A. Oredipe, R. F. Barth, S. E. Tuttle, D. M. Adams, I. Sautins, D. M. Bucci, C. M. Mojzisik, G. H. Hinkle, S. Jewell, Z. Steplewski, M. O. Thurston, and E. W. Martin, Jr., "Limits of sensitivity for the radioimmunodetection of colon cancer by means of a hand held gamma probe" *Int. J. Rad. Appl. Instrum. Part B. Nucl. Med. Biol.* **15**, 595–603 (1988).
15. P. O. Brown and C. Palmer, "The preclinical natural history of serous ovarian cancer: defining the target for early detection," *PLoS Med.* **6**(7), e1000114 (2009).
16. H. Hayashi, K. Ashizawa, M. Uetani, S. Futagawa, A. Fukushima, K. Minami, S. Honda, and K. Hayashi, "Detectability of peripheral lung cancer on chest radiographs: effect of the size, location and extent of ground-glass opacity," *Br. J. Radiol.* **82**(976), 272–278 (2009).
17. A. Bozzini, G. Renne, L. Meneghetti, G. Bandi, G. Santos, A. R. Vento, S. Menna, S. Andriguetto, G. Viale, E. Cassano, and M. Bellomi, "Sensitivity of imaging for multifocal-multicentric breast carcinoma," *BMC Cancer* **8**(1), 275 (2008).
18. M. Mancini, E. Vergara, G. Salvatore, A. Greco, G. Troncone, A. Affuso, R. Liuzzi, P. Salerno, M. Scotto di Santolo, M. Santoro, A. Brunetti, and M. Salvatore, "Morphological ultrasound microimaging of thyroid in living mice," *Endocrinology* **150**(10), 4810–4815 (2009).
19. N. A. Shkumat, A. Springer, C. M. Walker, E. M. Rohren, W. T. Yang, B. E. Adrada, E. Arribas, S. Carkaci, H. H. Chuang, L. Santiago, and O. R. Mawlawi, "Investigating the limit of detectability of a positron emission mammography device: a phantom study," *Med. Phys.* **38**(9), 5176–5185 (2011).
20. C. Tang, P. J. Russell, R. Martiniello-Wilks, J. E. Rasko, and A. Khatri, "Concise review: Nanoparticles and cellular carriers-allies in cancer imaging and cellular gene therapy?" *Stem Cells* **28**(9), 1686–1702 (2010).
21. N. S. Makarov, M. Drobizhev, and A. Rebane, "Two-photon absorption standards in the 550–1600 nm excitation wavelength range," *Opt. Express* **16**(6), 4029–4047 (2008).
22. N. S. Makarov, E. Beuerman, M. Drobizhev, J. Starkey, and A. Rebane, "Environment-sensitive two-photon dye," *Proc. SPIE* **7049**, 70490Y (2008).
23. A. Rebane, M. A. Drobizhev, N. S. Makarov, E. Beuerman, C. Nacke, and J. Pahapill, "Modeling non-Lorentzian two-photon absorption line shape in dipolar chromophores," *J. Lumin.* **130**(6), 1055–1059 (2010).
24. V. P. Tokar, M. Y. Losytskyy, V. B. Kovalska, D. V. Kryvorotenko, A. O. Balanda, V. M. Prokopets, M. P. Galak, I. M. Dmytruk, V. M. Yashchuk, and S. M. Yarmoluk, "Fluorescence of styryl dyes-DNA complexes induced by single- and two-photon excitation," *J. Fluoresc.* **16**(6), 783–791 (2006).
25. R. Ramadass and J. Bereiter-Hahn, "Photophysical properties of DASPMI as revealed by spectrally resolved fluorescence decays," *J. Phys. B* **111**(26), 7681–7690 (2007).
26. R. B. Owens, H. S. Smith, and A. J. Hackett, "Epithelial cell cultures from normal glandular tissue of mice," *J. Natl. Cancer Inst.* **53**(1), 261–269 (1974).
27. K. G. Danielson, L. W. Anderson, and H. L. Hosick, "Selection and characterization in culture of mammary tumor cells with distinctive growth properties *in vivo*," *Cancer Res.* **40**(6), 1812–1819 (1980).
28. L. W. Anderson, K. G. Danielson, and H. L. Hosick, "Metastatic potential of hyperplastic alveolar nodule derived mouse mammary tumor cells following intravenous inoculation," *Eur. J. Cancer Clin. Oncol.* **17**(9), 1001–1008 (1981).
29. S. L. Schor, "Cell proliferation and migration on collagen substrata *in vitro*," *J. Cell Sci.* **41**, 159–175 (1980).
30. H. Birkedal-Hansen and K. Danø, "A sensitive collagenase assay using [³H] collagen labeled by reaction with pyridoxal phosphate and [³H] borohydride," *Anal. Biochem.* **115**(1), 18–26 (1981).
31. R. C. Hallows, E. S. Bone, and W. Jones, "A new dimension in the culture of human breast," in *Tissue Culture in Medical Research II*, R. J. Richards and K. T. Rajan, eds. (Pergamon, Oxford, 1980), pp. 213–220.
32. N. P. Robertson, J. R. Starkey, S. Hamner, and G. G. Meadows, "Tumor cell invasion of three-dimensional matrices of defined composition: evidence for a specific role for heparan sulfate in rodent cell lines," *Cancer Res.* **49**(7), 1816–1823 (1989).
33. W. Jones and H. L. Hosick, "Collagen concentration as a significant variable for growth and morphology of mouse mammary parenchyma in collagen matrix culture," *Cell Biol. Int. Rep.* **10**(4), 277–286 (1986).
34. M. R. Lugo and F. J. Sharom, "Interaction of LDS-751 with P-glycoprotein and mapping of the location of the R drug binding site," *Biochemistry* **44**(2), 643–655 (2005).
35. "Primer3," <http://frodo.wi.mit.edu/primer3/input.htm>.
36. "ImageJ," <http://rsbweb.nih.gov/ij/>
37. C. D. M. Fletcher, ed., *Diagnostic Histopathology of Tumors* (Churchill Livingstone, 2007).

38. P. D. Eckford and F. J. Sharom, "P-glycoprotein (ABCB1) interacts directly with lipid-based anti-cancer drugs and platelet-activating factors," *Biochem. Cell Biol.* **84**(6), 1022–1033 (2006).
-

1. Introduction

Optical imaging of cancer is becoming an increasingly useful instrument for refining early diagnosis [1–4], developing targeted therapies [5,6] and monitoring of patient response to therapy [1,7]. However, operating either as a unimodal [8,9] or a hybrid technique [10], imaging in the visible region of the spectrum currently suffers from poor light penetration of the tissues. On the other hand, in the near-IR wavelength region (700–1200 nm) the tissues absorb and scatter light much less than in the visible range, allowing imaging of tumors down to several cm depths [11,12].

Various estimates place the minimal cancer cell count, i.e. the limit where the tumor becomes clearly detectable, between $\sim 5 \times 10^5$ and $\sim 10^9$ cells [13–15]. Such a wide variation results from many circumstances including different tumor histiotypes, different tumor morphologies, different anatomical locations and whether or not there exist any preclinical markers (such as the BRCA1 gene). Most current imaging techniques have stated minimal tumor sizes for detection that lie between 2 and 6 mm diameter [13,16–19], which corresponds to the late preclinical stage of malignancy. Frequently, minimally detectable tumors are significantly larger than this, especially if the location is deeper inside the tissue [17,20]. Therefore, increasing the detection sensitivity is essential for improving treatment outcomes. In this paper we describe novel imaging protocols that could be useful in early cancer detection, and, perhaps, also in monitoring dormant cancer deposits.

Two-photon excited fluorescence (2PEF) offers potential improvements over conventional one-photon excitation techniques, which include better 3D resolution, higher depth efficacy, higher specificity and lower scattering. Despite these advantages, few chromophores have been developed for use in tissues in the near-IR region. Indocyanine green has been approved for imaging in patients for some time, and most potential alternative dyes are related cyanine compounds. Styryl-9M is a water-soluble commercial dye that has efficient near-IR fluorescence and possesses large 2-photon absorption (2PA) cross section, $\sigma_2 = 750$ GM at 1200 nm [21]. In our preliminary studies we have shown that Styryl-9M is particularly sensitive to its local environment under 2-photon hyperspectral conditions [22], which is related to the fact that this chromophore possesses a large change of the permanent electric dipole moment between the ground and the first excited state, $\Delta\mu = 25$ D [23]. In addition, the Styryl dyes are known to be biocompatible [24,25] and so make a good starting point for developing 2-photon imaging agents for use in the tissue transparency region. Most diagnostic methods are not sensitive enough to detect the minimum diagnostically relevant number of malignant cells in tissues. In this publication, we develop a novel *in vivo* dual-wavelength near-IR imaging technique that uses two-photon excitation of fluorescence of Syryl-9M by loosely focused 1 kHz repetition rate high peak intensity femtosecond laser pulses. In comparison to commonly utilized laser-scanning mapping mode with tight focus, the wide-field mode facilitates easier access to deeper tumors. We show that under these conditions Syryl-9M can detect as few as 10 cells in a biologically relevant phantom. This outstanding characteristic should bode very well for development of new highly efficient near-IR clinical imaging agents.

2. Methods

2.1. Cells and cell culture

For our collagen gel phantom experiments, we required cell lines that we knew from experience would not be adversely affected by culturing in three dimensional collagen type I gels. This was true of all the cell lines used in this work. Three of the lines, normal mammary, +SA and 4T1, were also derived from the same BALB/c inbred mouse strain. The MDA-MB-231 and NIHovcar3 cells were chosen to represent malignant human cell lines. Passage

two, normal mouse mammary epithelial cells were propagated from cells obtained from Dr. H. L. Hosick in 1974, and subsequently stored in liquid N₂. The stocks were given to Dr. Hosick by Dr. A. J. Hackett [26]. They were propagated in tissue culture flasks coated with a dilute solution of Collagen Type IV (isolated by us from the EHS tumor). The medium used was DMEM:F12 (HyClone Thermo Fisher Scientific, Waltham, MA) supplemented with 10% (v:v) fetal bovine serum (HyClone Thermo Fisher Scientific, Waltham, MA), 2 µm/ml L-glutamine, 20 µg/ml gentamicin and ITS (insulin, transferrin and selenium supplement) as recommended by the manufacturer (Invitrogen). The same medium was conditioned by exposure for two days to logarithmically growing mouse 4T1 mammary carcinoma cells and subsequently filtered through 0.2µ pore sized filters. This conditioned medium was used at 25% (v:v) to facilitate the propagation of the normal mouse mammary epithelial cells. +SA mammary carcinoma cells were propagated from frozen stocks obtained from Dr. Hosick in 1986. These are a subline derived from the WAZ-2T tumorigenic line of the BALB/c mouse. Less than 1% WAZ-2T cells were able to produce colonies in soft agar culture [27]. Two soft agar colonies were picked and used to generate the +SA line. Characterization of early passages of +SA cells showed that they represented malignant, mouse mammary carcinoma cells [28]. The 4T1 mouse mammary carcinoma cell line was obtained from the ATCC, and represents highly malignant, aggressive mouse mammary carcinoma cells. Its behavior in BALB/c mice is very reminiscent of aggressive malignant mammary carcinomas in women. The MDA-MB-231 human mammary carcinoma cell line and the NIH-OVCAR3 human ovarian carcinoma line were both obtained from the ATCC, and, in our hands, give rise to malignant tumors in *SCID* mice. All cell lines, with the exception of the normal mouse mammary epithelial cells, were grown in tissue culture plastic flasks (TPP, Techno Plastic Products, CH-8219 Trasadingen, Switzerland) on the unmodified tissue culture surface, using the medium described above without the addition of any conditioned medium. For subculture, the cell monolayers were washed with Ca²⁺- and Mg²⁺-free Tyrode's balanced saline, then exposed for 2 to 5 minutes to Ca²⁺- and Mg²⁺-free Tyrode's balanced saline containing 0.05% trypsin and 0.02% EDTA until the cells loosened from the substrate, followed by the addition of serum containing medium to inhibit further trypsin activity. Cell lines were subcultured weekly and cells were incubated at 37°C in a humidified atmosphere of 7% CO₂ in air.

2.2. Preparation of collagen Type I based phantoms

Rat tail collagen type I was isolated by us using methods developed from the procedures described by Schor [29], Birkental-Hansen and Dano [30], and Hallowes et al. [31]. Our methods are described in detail in [32]. The collagen solution was used at a concentration of 1mg/ml in sterile deionized water and was stored at 4°C. Because acid solutions were used to isolate the collagen, the final collagen solution was also very slightly acidic, which prevented premature gelling. A slightly alkaline setting solution containing concentrated base medium and hepes buffer [33] was used to initiate collagen gelling. To provide a more biologically relevant phantom, 1mg/ml bovine hemoglobin (Sigma-Aldrich, St. Louis, MO) was added to the collagen setting solution. Phantoms were prepared by mixing 1.5 ml collagen type I with 0.3 ml setting solution with or without 0.2 ml of complete medium containing 10⁵ cells. The mixture was rapidly poured into a sterile polystyrene disposable fluorescence cuvette (Sigma-Aldrich, St. Louis, MO) and allowed to stand for 30 minutes in room atmosphere. One and a half ml of serum and phenol red -free medium was layered over the collagen gel, and the phantom was then incubated, until used, at 37°C in a humidified atmosphere of 7% CO₂ in air. Medium and buffers containing phenol red were avoided when collecting imaging data.

For imaging of cancer cell colonies, a phantom containing uniformly dispersed normal mammary epithelial cells was first prepared as described above, and, while the gel was still semi-set, an appropriate number of tumor cells were injected into the gel using a 1µl (lower concentrations $\leq 10^3$) or 10µl (cell concentrations $> 10^3$) micropipette tip. To ensure repeatability of the injection procedure a template with an offset opening matching the

micropipette tip was placed on the top of the cuvette. The template allowed us to better locate and align the tumor colony relative to the imaging apparatus. Staining of the phantom was accomplished by adding 7 μ l of a 10 mg/ml solution of Styryl-9M in DMSO to the medium above the gel. The dye was allowed to diffuse downwards throughout the gel matrix during an overnight incubation, after which the phantom was imaged.

The properties of the phantoms are illustrated in Fig. 1. Panel (a) shows a general view of a collagen type I based phantom positioned in the cuvette holder used for imaging. Panel (b) shows a normal mouse mammary epithelial cell colony in a phantom after 2 days of incubation. Panel (c) shows a normal mouse mammary epithelial cell colony after 14 days of incubation; photographed using a Nikon Diaphot inverted phase contrast microscope (X375).

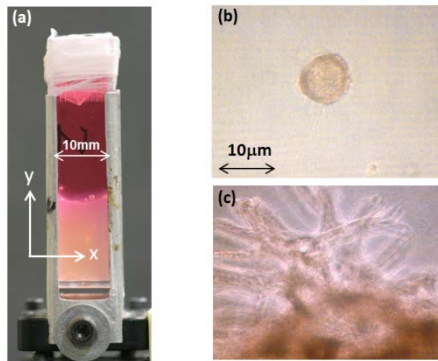


Fig. 1. Properties of the tissue phantoms. (a) General view of a collagen type I based phantom consisting of collagen matrix (lower half) and serum medium containing Styryl-9M (upper half); (b) a normal mouse mammary epithelial cell colony in a phantom after 2 days of incubation; (c) high magnification image of normal mouse mammary epithelial cell colony after 14 days of incubation.

2.3. Preparation of mice with tumor colonies in the external ear

4T1 cells were grown in tissue culture to late log phase (about 80% confluent). The cells were then harvested as described earlier. Balb/c female mice were anesthetized using isofluorane in oxygen. 4T1 cells, 10^5 in 0.05 ml of serum free medium, were injected subcutaneously in the pinna of one ear using a glass 0.25 ml syringe and a 27 gauge needle. Styryl-9M in DMSO was diluted in serum free medium as described above and applied to both sides of the pinna 16 hours before imaging the tumor colonies.

2.4. Isolation of RNA and real-time PCR

When considering possible reasons for our different results staining normal and malignant cells with Styryl 9M, we noted that a related styryl dye, LDS-751, had been clearly demonstrated to bind to the drug efflux pump p-glycoprotein, giving rise to enhancement of its fluorescence [34]. The two human cancer cell lines would likely show an elevation in their expression of drug efflux pumps, because the patients, from whom they were isolated, would probably have received some chemotherapy. Elevations of drug efflux pump expression might not be expected for the mouse mammary cell lines for this reason. However, cancer and normal cell membranes are quite different in their compositions. Lipid changes, in particular, would be expected to lead to fluorescence changes for Styryl 9M. In this study, we evaluate the expression of drug efflux pump MDR1 proteins to gain some information relevant to this question.

For each cell line, two 150 x 20 mm tissue culture dishes were grown to near confluence. The medium was removed and the cell monolayers rapidly washed with serum free medium. Three ml of Tri-reagent (Life Technologies Corporation, Carlsbad, Calif.) was added to each

dish and RNA was immediately isolated following the instructions of the manufacturer. Isolated RNA was stored at -80°C till use. RNA concentrations were determined by spectrophotometry, and RNA integrity was assessed using an Agilent 2100 bioanalyzer (Agilent Technologies, Santa Clara, Calif.). All samples scored at least 8/10 for overall integrity. Reverse transcription was conducted using the Ambion (Life Technologies Corporation, Carlsbad, Calif.) Retroscrip C kit with random decamer primers following the manufacturer's instructions. Amplification for specific products was then carried out using the SybrGreener kit from Invitrogen (Life Technologies Corporation, Carlsbad, Calif.) on a Corbett 3000 real-time PCR instrument (Quiagen, Valencia, Calif.). The MDR1 primers were designed using the Primer3 Web interface [35]. Primer sequences are shown in Table 1. At the end of each amplification run, the melt profiles were generated for each amplicon to assess the quality of the target sequence amplification. Roto-Gene series 6000 software (Quiagen, Valencia, Calif.) was used to quantitate the amounts of target sequences relative to the housekeeping genes, HPRT, GAPDH, or RPL23. MDR1 primers and validated housekeeping gene primers were synthesized by Integrated DNA Technologies (San Diego, Calif.).

2.5. Immunostaining of cells for p-glycoprotein

Cells were grown to near confluence on glass cover slips. For staining, the cover slips were washed quickly in excess phosphate buffered saline containing 2% bovine serum albumin before being fixed in acetone and air dried. The cover slips were then stored at -80°C . The primary antibody used was an affinity purified rabbit anti-p-glycoprotein antibody purchased from Abiotech (San Diego, Calif.), and was used at a dilution of 1:100 in phosphate buffered saline containing 2% bovine serum albumin. After primary antibody staining and subsequent washes in phosphate buffered saline containing 2% bovine serum albumin, protein A Alexa Fluor 568 (Life Technologies Corporation, Carlsbad, Calif.) at a 1:200 dilution was used to label the bound anti-p-glycoprotein. SYBR Green (Life Technologies Corporation, Carlsbad, Calif.) was used as a nuclear counterstain. Control preparations either had no primary antibody or no protein A. The stained cells were examined on a Nikon Eclipse microscope with images acquired using Metamorph (Molecular Devices, Sunnyvale, Calif.). Collection times were 30 ms for green fluorescence and 60 ms for red fluorescence. Image J [36] was later used to quantitate the average red fluorescence per cell.

2.6. Imaging instrumentation

A schematic of the imaging setup is shown in Fig. 2. The sample was set on a three-axis adjustable translation stage and comprised either tissue phantom in $1 \times 1 \text{ cm}$ spectroscopic cuvette or the external ear of an anesthetized mouse. To excite the two-photon induced fluorescence we used near-IR femtosecond optical parametric amplifier (TOPAS-C, Light Conversion), which produced $\sim 100 \text{ fs}$ duration pulses at 1 kHz repetition rate and $\sim 100 \text{ mW}$ average power. The wavelength of the OPA could be tuned continuously in the range 800-1600 nm (combined signal and second harmonic of idler). As the pumping source for the OPA we used pulses (795 nm peak wavelength, 150 fs duration, 1 W average power) from Ti:sapphire regenerative amplifier (Legend-HE Coherent), which itself was seeded by Coherent Mira 900 femtosecond mode-locked Ti:sapphire laser. The laser beam was passed through a variable neutral density filter and an iris diaphragm and was focused with a $f = 10 \text{ cm}$ lens about 1 cm behind the sample. The diameter of the beam (FWHM) at the sample was $\sim 200 \mu\text{m}$. The average incident power on the phantom as well as on the mouse ear was $\sim 8\text{-}10 \text{ mW}$ at 1100 nm and $\sim 9\text{-}11 \text{ mW}$ at 1200 nm. No photobleaching or photodamage of the fluorescent dye was observed. The fluorescence excited in the sample was imaged on a thermo-electrically cooled CCD detector (Xillix MicroImager PMI1400) in the direction perpendicular to the excitation beam using either a 75-mm f/1.4 objective lens or a microscope objective. In the case of phantom imaging, the sample was placed at distance ~ 28

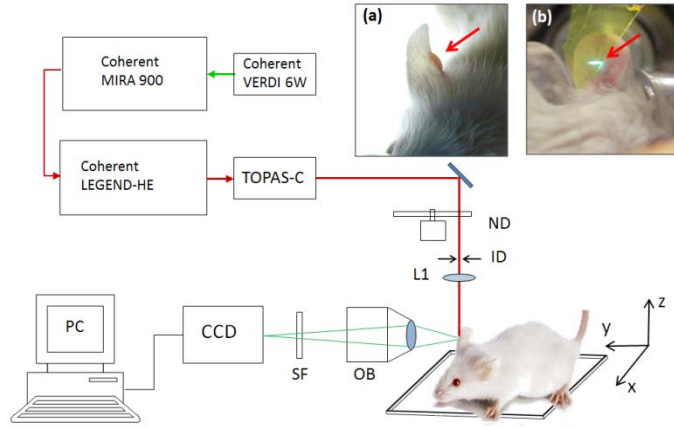


Fig. 2. Schematic of the imaging setup. ND, variable neutral density filter; ID, iris diaphragm; L1, focusing lens; OB, imaging objective (camera lens or microscope objective); SF, spectral filter; CCD, imaging detector. Inserts show the mouse ear tumor (a) and the near-IR laser spot (b); 2PEF in a dye-doped plastic film positioned in front of the tumor visualizes the laser beam.

cm from the CCD input, such that the field of view of the camera lens was about ~2 cm wide. For imaging of the mouse ear an extension tube was added between the objective and the CCD, which provided an additional 5x magnification and also reduced the corresponding field of view to ~4 mm. Further magnification along with corresponding reduction of the field of view to ~3 mm was achieved when the camera objective was replaced by a 4x microscope objective. A stack of color spectral filters or a liquid-crystal spectral filter (VariSpec, CRi, Woburn, MA) was placed in front of the CCD. The filters were selected to pass the fluorescence wavelength of the Styryl-9M dye (730-820 nm) while blocking the near-IR scattered laser light.

The mouse was anesthetized with isofluorane in oxygen using a face mask and an anesthetic machine. The respiration rate was detected using a small pressure detector and displayed on a monitor outside the imaging box.

3. Results and discussion

3.1. 2PEF imaging of tissue phantoms

Figure 3(a) shows the two-photon absorption (2PA) spectrum of Styryl-9M in chloroform measured by standard fluorescence excitation method [21]. The 1PA extinction spectrum and the fluorescence emission spectrum are shown for comparison. The broad and intense peak at 1100 – 1400 nm corresponds to the $S_0 \rightarrow S_1$ transition in the one-photon absorption (1PA) spectrum and is associated with the strongly dipolar nature of this molecule [23]. Our recent measurements [22] have shown that both the 1PA and 2PA spectra experience a large bathochromic shift with increasing solvent polarity, up to $\sim 3000 \text{ cm}^{-1}$ with the change of the solvent polarity function from 0.35 to 0.5. The fluorescence emission intensity also changed significantly when the pH of the aqueous solution was varied from 8 to 11 [22]. This evidence suggests that Styryl-9M has high sensitivity to its local environment. Figure 3(b) shows the relative 2PEF spectrum measured as a function of the excitation laser wavelength in three different tissue phantoms. To quantify the observed differences, we normalize the data points such that at the shorter laser excitation wavelengths, $\lambda_{\text{ex}} < 1100 \text{ nm}$, the spectra essentially overlap. At $\lambda_{\text{ex}} = 1200 \text{ nm}$, the sample with the normal cells shows 20% higher signal (relative to $\lambda_{\text{ex}} = 1100 \text{ nm}$) compared to the reference sample containing no cells and the phantom with +SA cancer cells shows 80% higher relative fluorescence.

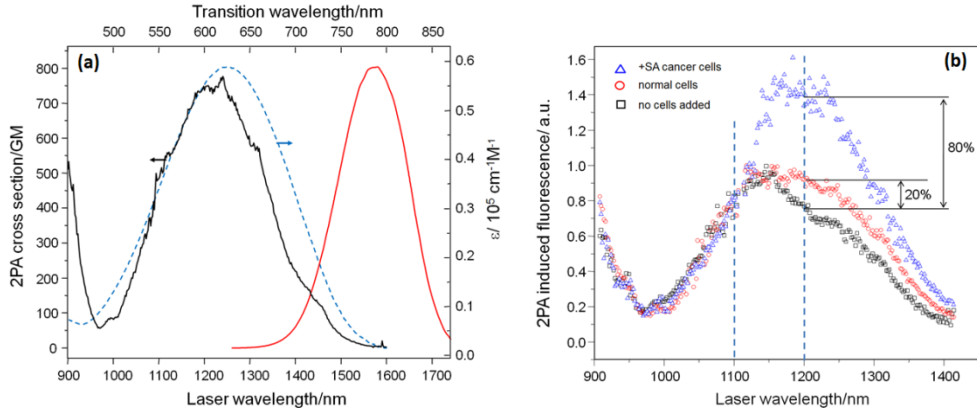


Fig. 3. (a) 2PA spectrum of Styryl-9M in chloroform (black line), shown as 2PA cross section (left y-axis) versus laser wavelength (bottom x-axis). 1PA extinction spectrum (blue dotted line) and fluorescence emission spectrum (red line) in chloroform; (b) 2PEF spectra in tissue phantoms with no cells (black squares), with normal cells (red circles), and with cancer cells (blue triangles), all normalized at 1100 nm and presented in arbitrary units.

In the following experiments, we use the large ratiometric difference in the 2PEF spectra at 1100 and 1200 nm to distinguish between normal cells and cancer cells.

3.2. Dual wavelength 2PEF imaging of different types of cancer colonies

For a particular pixel of the CCD detector with coordinates x_i, y_j , the ratio of the fluorescence intensities excited with 1100- and 1200-nm pulses, $I_{1100}(x_i, y_j)$ and $I_{1200}(x_i, y_j)$, is given by

$$F(x_i, y_j) = \frac{I_{1200}(x_i, y_j)}{I_{1100}(x_i, y_j)}. \quad (1)$$

Because the relative 2PEF at 1100 nm does not depend on the composition of the phantom, the ratio given by Eq. (1) effectively discriminates the pixel corresponding to the cancer cells from those where the signal originates from the normal cells (or with no cells). In practice, the images depend on the laser powers at 1100 nm (P_{1100}) and 1200 nm (P_{1200}) and also contain background signal and noise. To take these effects into account, we define the normalized fluorescence intensity ratio function as follows:

$$\tilde{F}(x_i) = \frac{I_{1200}(x_i) - I_B(x_i)}{I_{1100}(x_i) - I_B(x_i)} \left(\frac{P_{1100}}{P_{1200}} \right)^2, \quad (2)$$

which considers an integrated intensity over the spatial direction perpendicular to the laser beam (x) and observation (z) directions:

$$I(x_i) = \sum_{j=1}^M I(x_i, y_j), \quad (3)$$

where M is the total number of pixels in y -direction. In Eq. (2), $I_B(x_i)$ is the background intensity (measured with the laser beam blocked).

Figure 4 shows the normalized fluorescence intensity ratio (2) measured in 5 different phantoms where x corresponds to the laser beam propagation direction. The first two phantoms shown in Fig. 4(a), are homogeneous: One contains only normal cells (red symbols), and the other only the +SA cancer cells (blue symbols), uniformly in the collagen matrix in both cases. A small regular signal drift along x -direction is likely caused by increased scattering of the laser light within the sample. Figure 4(b) shows the fluorescence

signal observed in phantoms that contained mostly normal cells, simulating normal tissue background, with an implanted single cancer colony. Three different mammary cancer cell lines were used: MBA-MD-231, 4T1, and +SA. The spatial size ($\sim 10 \mu\text{m}^3$) and the cell count ($\sim 10^5$ cells) of each cancer colony were chosen to closely represent a typical case in a preclinical stage of malignancy. After a given number of tumor cells were introduced into the phantom, as described in Section 2, the phantom was incubated for one day before being stained and scanned. The colony was located near the center of the phantom. As described in Section 2, a template was used to ensure that the implanted colony was always placed in the phantom in the same location relative to the laser beam. The fluorescence ratio in Fig. 4(b) shows a well-defined feature at the location of the cancer colony. As expected, the fluorescence ratio increases at the location of the cancer cells, whereas, outside of the cancer colony, the signal drops to the background level corresponding to normal mammary cells. Figure 4(b) also shows that the imaged widths of the cancer colonies distributions are significantly narrower than those of real implants (vertical dashed margins in Fig. 4(b)) may be explained by the defocusing effect due to both the scattering of laser excitation beam and of the emitted fluorescence.

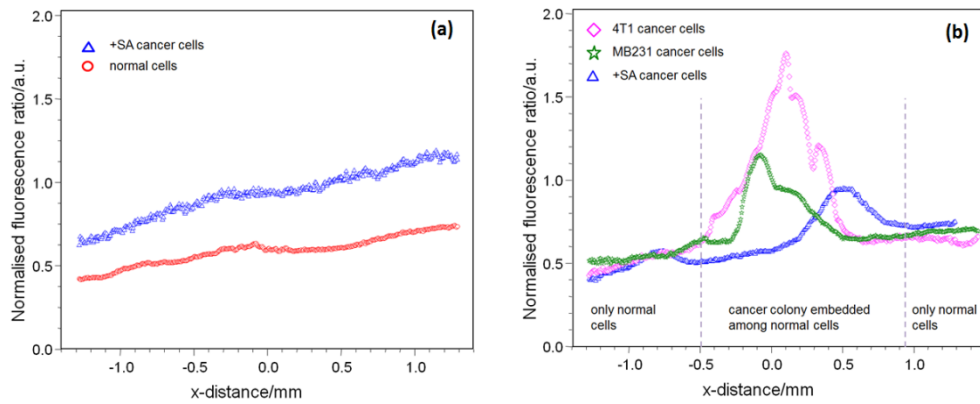


Fig. 4. Dependence of the fluorescence intensity ratio (2) on the x -distance across the phantom. (a) Homogeneous phantoms with uniform distribution of the cells throughout the collagen matrix. The coding of the colony types is shown in the inset. (b) Phantoms containing, in addition to normal cells, a single implanted colony of cancer cells. Distance is measured from the center of the phantom. Vertical dashed lines indicate approximate margins of the initially implanted cancer colony. The laser beam had a symmetrical Gaussian spatial profile with FWHM of $\sim 200 \mu\text{m}$. The excitation beam propagates from right to left.

3.3. Detection limits for the minimum number of cancer cells in phantoms

Our next step was to evaluate the ultimate detection sensitivity of this new method. In other words, how small a colony can we detect within a much larger pool of normal cells? For this purpose, a series of phantoms were prepared containing progressively fewer cancer cells, starting from 10^5 cells in a colony and going down to an estimated single cell. In this experiment, we used +SA and NIHOCAR3 cancer cell lines.

Figure 5 shows the peak value of the fluorescence ratio (2) at the colony location for a series of samples with different estimated cancer colony cell counts. At the higher cell counts, $>10^3$ per colony, the signal is well above the background level. With the decreasing number of the +SA cells, the signal drops and becomes indistinguishable from the background for 200–300 cells per colony. On the other hand, with decreasing number of NIHOCAR3 cells, the ratiometric fluorescence signature is clearly distinguishable even for as few as 10 cancer cells. The horizontal dotted line shows our empirical threshold for the fluorescence ratio used to discriminate between the samples diagnosed as cancer-containing, if the fluorescence ratio is above the threshold, or as healthy, if the fluorescence ratio is below the threshold.

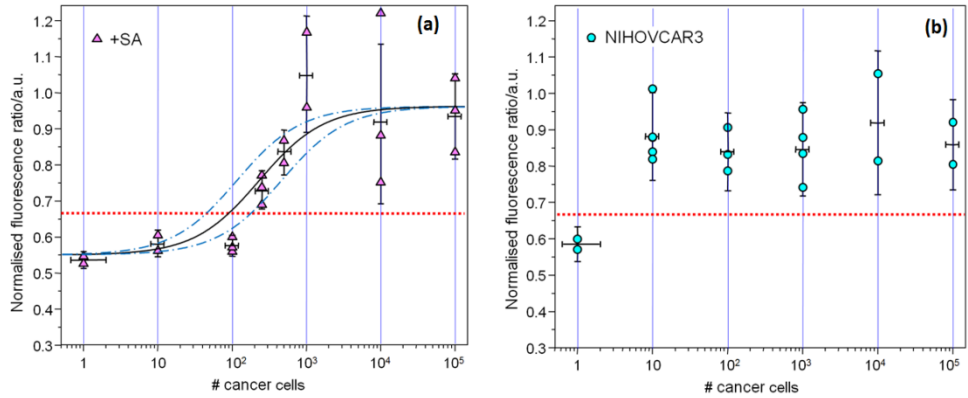


Fig. 5. Estimation of the smallest number of cancer cells that can be detected as a colony in the phantom. Horizontal axes – estimated number of cancer cells in the implanted colony; Horizontal dotted line indicates the empirical threshold for the discrimination between the cancer-containing and cancer-free samples; (a) +SA cancer line. Solid curve: fit parameters used, $F^U = 0.55$, $F^B = 0.95$, $N = 10^6$, $N_{P_{gp}} = 40,000$ and $\Delta E/kT = 16.0$; (b) NIHOCAR3 cancer line.

The minimal estimated numbers of the cancer cells detectable with our new method are well in the range that would produce a significant impact for improved cancer diagnostics. Of course, the results for actual tissues might not be as good as for our phantoms, especially given that real tissues would show increased light scattering. However, even with this in mind, our result in collagen type I based phantoms with NIHOCAR3 cells indicate possibility of extremely low minimal detection limits. Of course, detecting individual cancer cells is a standard procedure in histopathology [37], where single cancer cells are routinely identified based on the well-established morphological differences from the normal cells in stained tissue samples. However, traditional histopathology requires an actual biopsy, which is an invasive procedure. Our current result, which might be also called optical biopsy, is remarkable in the sense that we can optically detect small numbers of living cells in a three-dimensional environment, quite similar to their natural *in vivo* environment, with only a simple stain used in a non-invasive manner. For comparison, currently available non-invasive fluorescent techniques [1,6] are able to detect malignant tissues only if they contain more than 10^5 – 10^7 cancer cells.

3.4. MDR1 expression profiles for the cells used in this study

The data for the relative protein and mRNA expression for MDR1 proteins for all the cell lines used in this study are collected in Tables 1–3. Table 2 shows the relative fluorescence for MDR1 for all mammary cell lines used; Table 3 shows the real-time PCR expression analysis for MDR1 proteins and Table 1 shows the primers used in the real time PCR analysis. Figure 6 shows the microscope image of 4T1 cell sample in the fluorescent immunostaining for MDR1 proteins.

Fluorescence resulting from staining with anti p-glycoprotein and protein A coupled to Alexa Fluor 568 was clearly present in the cytoplasmic/membrane portions of all the cell lines. Images captured with Metamorph (Fig. 6) and analyzed with Image J, demonstrated that 4T1 showed the most fluorescence, while MDA-MB-231, +SA and normal mouse mammary epithelial cells showed progressively less fluorescence (Table 2). Therefore, on a protein based level, 4T1 cells can be regarded as relatively high expressors of MDR1. Table 1 and 2 show the results of the real-time PCR experiments to compare the mRNA expression profiles for MDR1 proteins. Of the two human cancer cell lines examined, NIHOCAR3 and MDA-MB-231, NIHOCAR3 exhibited significantly higher expression of MDR1 mRNA. For the

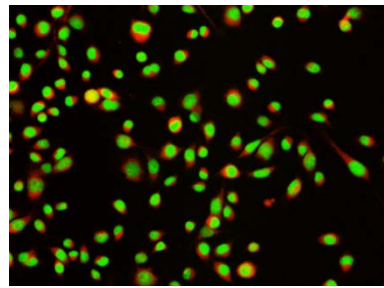


Fig. 6. Fluorescence image of 4T1 cells stained with anti p-glycoprotein antibody and Alexa Fluor 568 protein A.

murine cell lines, for both MDR1A and MDR1B, the normal mouse mammary epithelial cells exhibited the least mRNA expression, while the two carcinoma lines, +SA and 4T1 exhibited similar higher levels. Comparative housekeeping genes were chosen to best match the average levels of the gene transcript being evaluated. LDS-751 (Styryl-8), has a very close structure to Styryl-9M and is known to be bound by p-glycoprotein leading to a spectral shift for the dye [34]. If, as is likely, Styryl-9M is also bound by p-glycoprotein, we might expect the positive correlation of increased spectral shift with p-glycoprotein expression and malignancy, seen in this article.

Table 1. Primers used in the real time PCR analysis

<i>Gene transcript</i>	<i>Forward primer</i>	<i>Reverse primer</i>
Human MDR1 long	TGACATTATTCAAAGTAAAAGC	TAGACACTTTATGCAACATTCAA
Human MDR1 short	AAATTGGCTTGACAAGTTGTATATGG	CACCAGCATCATGAGAGGAAGTC
Mouse MDR1A	AAATTGGCTTGACAAGTTGTATATGG	TGTGCTCTCTCCCGCAGCCAC
Mouse MDR1B	AAATTGGCTTGACAAGTTGTATATGG	CTCGGCCATCGTGGTGGCAA
Human HPRT	Validated primers from Integrated DNA Technologies	
Human GAPDH		
Mouse RPL23		

Table 2. Relative fluorescence for MDR1

<i>Cell line</i>	<i>Average p-glycoprotein fluorescent signal</i>
4T1	24.2
MDA-MB-231	17.3
+SA	4.6
Normal mouse mammary epithelium	2.2

Table 3. PCR expression analysis for MDR1 proteins

<i>Cell line</i>	<i>Gene transcript</i>	<i>Relative expression normalized to the housekeeping gene</i>	<i>Housekeeping gene</i>
MDA-MB-231	MDR1 long	00.19	HPRT
NIHOVCAR3	MDR1 long	00.94	HPRT
MDA-MB-231	MDR1 long	00.31	GAPDH
NIHOVCAR3	MDR1 short	18.10	GAPDH
Norm. mouse mam. epith.	MDR1A	00.52	RPL23
+SA	MDR1A	03.93	RPL23
4T1	MDR1A	03.36	RPL23
Norm. mouse mam. epith.	MDR1B	05.56	RPL23
+SA	MDR1B	16.10	RPL23
4T1	MDR1B	12.40	RPL23

3.5. Evaluation of the binding energy of Styryl-9M to the cancer cell membrane

It was noted above that the dependence of 2PEF of Styryl-9M on different solvent polarity may be presented as a superposition of two distinct spectral forms [22], where the shorter wavelength excitation peak is due to the Styryl-9M dissolved in water, whereas the longer wavelength peak may be associated with a less polar environment [22]. Even though the

spectral signatures obtained from the tissue phantoms (Fig. 3(b)) are less distinct than in simple solvents, it is still likely that the difference in the fluorescence intensity resulting from the 1100 nm and 1200 nm excitation is caused by different local environments. In particular, such a difference may arise if the dye preferentially adheres to some specific membrane sites on the cancer cells such as p-glycoprotein receptors. These receptors belong to the class of so-called drug-efflux proteins, which are often overexpressed by cancer cells in response to therapeutic drugs, while in most normal tissues the p-glycoprotein receptor numbers are lower [38]. Therefore, it is reasonable to assume that, at 1100 nm excitation, the fluorescence has a larger contribution from the Styryl-9M molecules dissolved in the surrounding medium (unbound form), whereas at 1200 nm excitation, relatively more fluorescence originates from the dye molecules attached to the cancer cells (bound form).

With the above assumptions, the normalized ratio of the fluorescence intensities detected at the two excitation wavelengths may be expressed as (for $P_{1100} = P_{1200}$)

$$F = \frac{\sigma_2^B(1200)\phi^B N^B + \sigma_2^U(1200)\phi^U N^U}{\sigma_2^U(1100)\phi^B N^B + \sigma_2^U(1100)\phi^U N^U}, \quad (4)$$

where $\sigma_2^B(\lambda)$ and $\sigma_2^U(\lambda)$ are the 2PA cross sections of the bound- and unbound forms at the corresponding excitation wavelength, ϕ^B and ϕ^U are the effective fluorescence quantum yields including the fluorescence collection and detection efficiency, and N^B and N^U are the numbers of the bound- and unbound dye molecules in the excitation volume. Earlier we have defined the effective fluorescence quantum yields such that at 1100 nm the two signals match:

$$\sigma_2^B(1100)\phi^B = \sigma_2^U(1100)\phi^U. \quad (5)$$

The above relations allows us to recast the normalized fluorescence ratio in the form

$$F = \frac{\sigma_2^U(1200)}{\sigma_2^U(1100)} + \frac{N^B}{N} \left(\frac{\sigma_2^B(1200)}{\sigma_2^B(1100)} - \frac{\sigma_2^U(1200)}{\sigma_2^U(1100)} \right), \quad (6)$$

where N is the total number of the dye molecules, $N = N^a + N^b$.

The equilibrium distribution between the dye molecules in the bound- and unbound states is governed by the equation

$$e^{-\frac{\Delta E}{kT}} = \frac{N^B}{(N - N^B)(N_{Pgp}N_c - N^B)}, \quad (7)$$

where N_c is the number of cancer cells in the colony, N_{Pgp} is the average number of receptors per cancer cell, ΔE is the binding energy (if the change in entropy is disregarded for hindered motion of a dye inside the viscous phantom). By solving Eq. (7) with respect to N^B and substituting the resulting value into (6), we find the following expression for the normalized fluorescence ratio as a function of the number of cancer cells:

$$F(N_c) = F^U + (F^B - F^U) \frac{1 + (N + \bar{N}_{Pgp}N_c)e^{-\frac{\Delta E}{kT}} - \sqrt{[1 + (N + \bar{N}_{Pgp}N_c)e^{-\frac{\Delta E}{kT}}]^2 - 4N\bar{N}_{Pgp}N_c e^{-\frac{2\Delta E}{kT}}}}{2Ne^{-\frac{\Delta E}{kT}}}, \quad (8)$$

where F^U and F^B are the fluorescence ratio values, respectively, if there are no cancer cells and if all dye molecules are bound. The solid line in Fig. 5(a) shows the best fit of the measured dependence on the number of +SA cancer cells, where $F^U = 0.55$ and $F^B = 0.95$ correspond to the extreme left and to the extreme right side of the graph. The best fit value for the binding energy is, $\Delta E/kT = 16.0 \pm 0.5$, which lies in a reasonable range for non-covalent

bonding. The dash-dotted curves above and below the solid curve in Fig. 5(a) indicate the estimated uncertainty of the binding energy value. Other two best fit parameters for the total number of the dye molecules is, $N = 10^6$, and the number of the receptors in one cancer cell, $N_{Pgp} = 40,000$. We note that even though these values are quite plausible, it is hard to estimate independently how many dye molecules diffuse into the phantom. The fact that the experimental data seems to be consistent with the model may corroborate our hypothesis that the adherence of Styryl-9M to the cancer cells may be responsible for the observed concentration dependence. Alternatively, the saturation of the fluorescence ratio at high cell counts may be also caused by quenching of the fluorescence, e.g., if more than one dye molecule becomes attached to the same site. Unfortunately, no meaningful fit for the NIHOCAR3 data could be obtained due to insufficient experimental data points.

3.6. Mouse ear imaging

The thin pinna of the mouse ear is an excellent site for initial *in vivo* imaging studies. Many malignant tumors will grow in this site, including the 4T1 murine mammary carcinoma (see Fig. 2), and access to the pinna is simple in an anesthetized mouse. When the animal is anesthetized, the rear 2/3 of the body can be immobilized in an appropriate diameter tube. The anesthetic is delivered by a face mask that does not extend to cover the external ears. When the laser beam was moved across an area of the pinna containing no obvious tumor, the only distortion of the fluorescence ratio occurred as the beam moved over the edge of the ear (Fig. 7(c)). In contrast, when the laser beam moved over an area of the pinna containing tumor tissue, while the distortion seen as the beam moved over the edge of the ear was again noted, a strong signal, in the opposite direction, was also seen at the position of the tumor (Fig. 7(d)). The signal resembled that found for tumor colonies in the phantom studies. Even though this is a very preliminary experiment, it is encouraging for the development of *in vivo* imaging using these protocols.

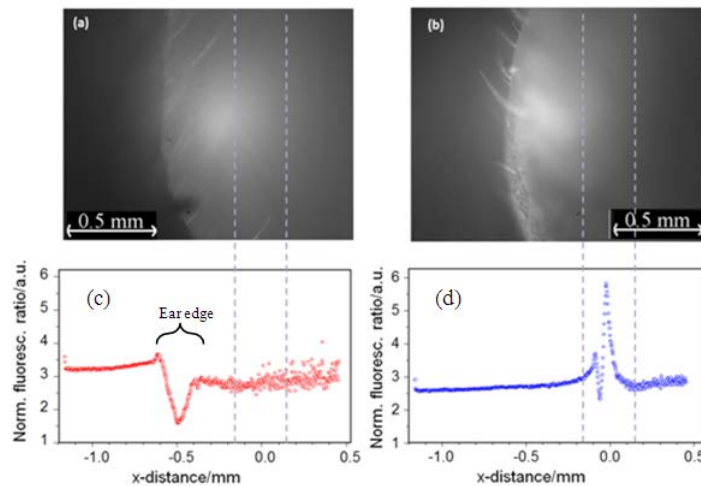


Fig. 7. Dual wavelength 2PEF imaging of the pinna of the mouse ear with the laser beam perpendicular to the pinna. Panels (a) and (c) show the image and the integrated intensity trace for an apparently normal region of the pinna of the ear; Panels (b) and (d) show the same for a region containing the 4T1 tumor.

As mentioned earlier, the tissue of the external ear is much denser than our collagen type I based phantoms. However, this did not degrade the relevant fluorescent signals, and a clear difference is seen between normal and cancer tissue. We have made no attempt to map the tumor within the ear using the fluorescent signals, but this is an obvious future direction, and one that will require significant software application. Success in such an endeavor would

constitute a first step towards image guided therapies. While the pinna of the ear is an excellent site for initial tissue studies, it does not provide any information as to the depth limitations of our approach in tissues. Our imaging technique should have good depth efficacy given that both the excitation and fluorescence emission wavelengths lie within the “tissue transparency window.” Depth efficacy studies are, also, obvious future directions for this project. Because of the positive correlation of MDR1 expression with the sensitivity of cancer detection in our imaging system, proof of Styryl-9 binding by p-glycoprotein needs to be sought, and the extent to which tumor malignancy can be correlated to Styryl-9 fluorescence parameters determined. Clinically, the possibility exists the Styryl-9 fluorescence parameters could provide a surrogate marker for likely multiple drug resistance.

4. Conclusions

To conclude, we have shown that a commercially available near-IR fluorescent organic dye, Styryl-9M, can be used for sensitive quantitative imaging of small cancer cell colonies embedded deep in biological tissue phantoms. Our method is based on the detection and quantitative analysis of the fluorescence signals obtained with two-photon excitation at two different wavelengths (1100 nm and 1200nm) in the near-IR range, where Styryl-9M shows a strong dependence of the 2PA and 2PEF on the local environment. We show that by calculating the normalized ration of the fluorescence intensity at 1200 nm and 1100 nm excitation wavelengths we achieve high sensitivity of detecting cancer cells surrounded by normal tissue cells. The two-photon fluorescence results showed a positive correlation with the levels of MDR1 proteins expressed by the cells, and for high MDR1 expressors, as few as ten cancer cells could be detected. Similar high sensitivity is also demonstrated for tumor colonies in mouse external ears. By comparing normalized ratios of the signal intensity at different wavelengths we are able to distinguish between samples with cancer cells, without cells, and with normal cells. We show that this dual wavelength ratiometric imaging allows, for first time, the spatial localization of as few as 10 cancer cells inside tissue phantoms. The proposed method seems promising for non-invasive optical detection of cancer. It can be applied for cancer diagnostics by differentiation of cancer vs. normal cells, as well as for precise localization of tumors.

Acknowledgments

We would like to acknowledge support from the Montana MBRCT Program and NIH Grant R01 GM098083. Also, we dedicate this manuscript to Dr. Howard L. Hosick, some of whose cell lines are used in this study. His premature death in March 2012 deprives us of an excellent colleague and friend.